Geochemistry Geophysics Geosystems G3
AN ELECTRONIC JOURNAL OF THE EARTH SCIENCES
Published by AGU and the Geochemical Society

Article
Volume 5, Number 12
15 December 2004
Q12006, doi:10.1029/2004GC000700
ISSN: 1525-2027

Heat flow through a basaltic outcrop on a sedimented young ridge flank

C. Geoffrey Wheat
Global Undersea Research Unit, University of Alaska Fairbanks, P. O. Box 475, Moss Landing, California 95039, USA (wheat@mbari.org)

Michael J. Mottl
Department of Oceanography, University of Hawaii, 1000 Pope Road, Honolulu, Hawaii 96822, USA (mmottl@soest.hawaii.edu)

Andrew T. Fisher
Earth Sciences Department and Center for the Study of Imaging and Dynamics of the Earth, University of California, Santa Cruz, California 95064, USA (afisher@es.ucsc.edu)

David Kadko
Division of Marine and Atmospheric Chemistry, Rosenstiel School of Marine and Atmospheric Sciences, University of Miami, 4600 Rickenbacker Causeway, Miami, Florida 33149, USA (dkadko@rsmas.miami.edu)

Earl E. Davis
Pacific Geoscience Centre, Geological Survey of Canada, P.O. Box 6000, Sidney, British Columbia, Canada V8L 4B2 (davis@nrcan.gc.ca)

Edward Baker
Pacific Marine Environmental Laboratory, NOAA, 7600 Sandpoint Way NE, Seattle, Washington 98115, USA (baker@pmel.noaa.gov)

[1] One hundred seven thermal gradients were measured in shallow surface sediments using the submersible *Alvin* within a 0.5 km^2 area on and around the 65-m-high, mostly sediment-covered Baby Bare outcrop located on the eastern flank of the Juan de Fuca Ridge. Heat flow values range from 0.35 W m^{-2}, which is close to the average value (0.27 W m^{-2}) for the sediment-buried 3.5-Myr-old crust surrounding the outcrop, to as high as 490 W m^{-2}. Some measurements are purely conductive, whereas others are consistent with upward fluid seepage through this sediment layer. Highest heat flow values are found roughly 10 m below the summit along a ridge-parallel fault where shimmering water, springs, and communities of clams were found. Heat flow values surrounding a second fault are elevated to a lesser extent (maximum of 9.2 W m^{-2}). The total power output from this 0.5 km^2 area is 1.5 MW, about 10 times greater than the conductive power output predicted for a commensurate area of 3.5-Myr crust. Much of this heat loss is conductive (~84%), consistent with an independent estimate of the convective heat flux from Rn/heat anomalies in spring fluids and in the water column above the springs. Calculations suggest that the 64°C isotherm, which is the temperature in the surrounding upper crust, is <20 m below the summit, corresponding to a height that is 30 m above the surrounding turbidite plain. These elevated fluid temperatures at shallow depths provide thermal buoyance to drive seafloor seepage from the outcrop.

Components: 10,761 words, 11 figures, 1 table.

Keywords: Baby Bare; heat flow; heat flux; hydrothermal; radon; ridge flanks.

Index Terms: 3015 Marine Geology and Geophysics: Heat flow (benthic) and hydrothermal processes; 5418 Planetology: Solid Surface Planets: Heat flow; 8424 Volcanology: Hydrothermal systems (8135).

Received 23 January 2004; **Revised** 29 July 2004; **Accepted** 16 September 2004; **Published** 15 December 2004.

Wheat, C. G., M. J. Mottl, A. T. Fisher, D. Kadko, E. E. Davis, and E. Baker (2004), Heat flow through a basaltic outcrop on a sedimented young ridge flank, *Geochem. Geophys. Geosyst.*, *5*, Q12006, doi:10.1029/2004GC000700.

1. Introduction

[2] One of the least known parts of global oceanic geochemical budgets is the contribution resulting from fluid transport and chemical exchange within the oceanic crust. Fluid flow is evident in many geologic settings, from mid-ocean ridges and flanks to subduction zones and continental margins. Of these settings the largest flow of seawater is through ridge flanks [e.g., *Sclater et al.*, 1980]. Patterns of seawater flow through the crust and exchange with the ocean are controlled by the distribution of permeability and driving forces, and are additionally influenced by basement relief, variations in sediment cover, and locations of basaltic outcrops, and exposed faults [e.g., *Lister*, 1972; *Fisher and Becker*, 1995; *Wang et al.*, 1997; *Fisher*, 1998; *Fisher et al.*, 2003a]. All of these factors are important at seamounts and at local basement highs that rise above the surrounding sediment plain. These fundamental features of seafloor topography are known to serve as crustal hydrothermal ventilators that may be active for millions of years [e.g., *Thompson*, 1983; *Davis et al.*, 1992; *Villinger et al.*, 2002; *Fisher et al.*, 2003b]. Understanding hydrogeologic processes within such features is necessary to quantify the role and vigor of circulation through ridge flanks and the effect of this circulation on geochemical budgets.

[3] One such active crustal ventilator is the Baby Bare basement outcrop located on 3.5-Myr-old crust east of the Juan de Fuca Ridge at 48°N [e.g., *Davis et al.*, 1992; *Mottl et al.*, 1998] (Figure 1). During an *Alvin* submersible cruise in 1995 we measured thermal gradients in the sediment on and around Baby Bare to (1) find locations where focused formation waters seep from the crust, (2) determine the heat flux, (3) constrain the subsurface thermal regime, and (4) assess the driving force in upper basement. Results from these analyses provide constraints for the longevity of the hydrothermal system at Baby Bare and the importance of ridge-flank venting on global scales. We also sampled the water column immediately above the springs and measured thermal and ^{222}Rn anomalies. These data coupled with chemical and thermal data from the springs allow us to make an independent estimate of the convective power output from the springs.

2. Geologic Setting

[4] Baby Bare is located ~101 km east of the active Endeavour Segment of the Juan de Fuca Ridge near 48°N (Figure 1). The seafloor expression of this basement outcrop, which extends above a flat turbidite plain, is about 1 km long, 0.5 km wide and 65 m high [*Becker et al.*, 2000]. The Baby Bare volcanic edifice lies on a buried ridge that extends for tens of kilometers in a north-northeasterly direction, and is roughly parallel to the active spreading ridge axis to the west. Another larger basement outcrop named Mama Bare is located along this ridge about 15 km northeast of Baby Bare. Ocean Drilling Program (ODP) Site 1026 was drilled through 229 m of sediment into igneous basement along this ridge about 6.3 km northeast of Baby Bare (Figure 1). Another basement ridge running parallel to the Baby Bare ridge is located ~7 km to the east. This ridge includes at least one basement outcrop (Papa Bare). ODP Site 1027 drilled through 614 m of sediment into a buried basement valley between these two ridges (Figure 1). High-resolution bathymetric and seismic surveys located two additional basement highs overlain by tens of meters of sediment (Wuzza Bare and Isita Bare) and two basement outcrops located 35 and 52 km to the southwest of Baby Bare (Grinnin' Bare and Grizzly Bare, respectively) [*Fisher et al.*, 2003a]. Sediment surrounding these ridges and outcrops is up to 700 m thick.

[5] The composition of basaltic glass recovered from Baby Bare is consistent with off axis formation [*Karsten et al.*, 1998]. In contrast, the underlying ridge formed by on-axis processes [*Davis et al.*, 1997a]; the Endeavour Segment is currently forming abyssal hills with similar relief [*Karsten et al.*, 1998]. On the basis of seismic reflection profiles and microfossil age data [*Davis et al.*, 1997a], *Becker et al.* [2000] suggest that Baby Bare is at least 1.7 Myr old, so all of the volcanic heat associated with outcrop emplacement should have dissipated. Thus the hydrothermal activity that we observed is a consequence of regional heating of basement formation fluids having a lithospheric origin.

[6] Several hydrothermal springs and associated communities of thysirid clams were found near

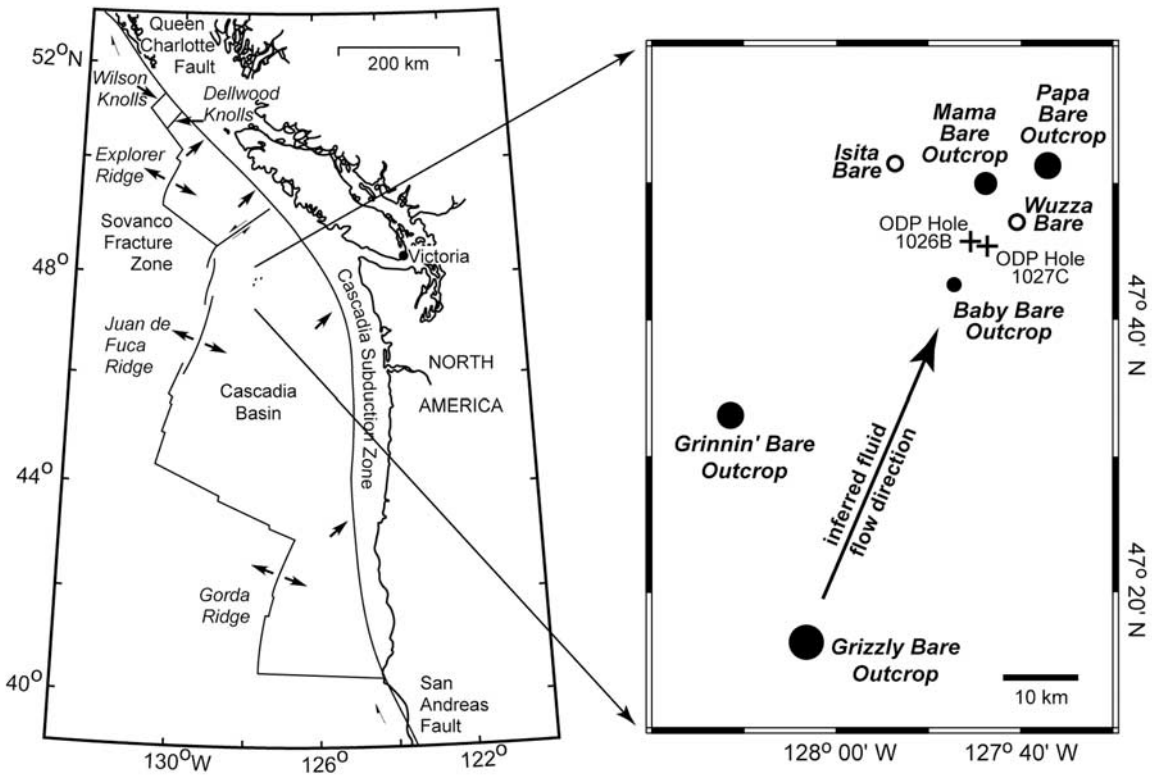

Figure 1. Baby Bare outcrop is located on the eastern flank of the Juan de Fuca Ridge overlying about 3.5-Myr-old crust. Basaltic outcrops (solid circles) and basement topographic highs are shown in the vicinity of Baby Bare. Baby Bare stands about 65 m above the sediment plain. Isita and Wuzza Bares (open circles) may have basaltic outcrop. Locations for ODP Sites 1026 and 1027 are indicated by a plus sign. The general path for fluid flow within basaltic basement is indicated by the direction of the arrow. Bottom seawater enters basement at Grizzly Bare and is warmed and altered during transport toward Baby and Mama Bares, where it vents to bottom seawater [*Wheat et al.*, 2000, 2002; *Fisher et al.*, 2003a].

the summit of Baby Bare [*Mottl et al.*, 1998]. Most of the springs are associated with a fault that strikes roughly parallel to the underlying ridge and to the active spreading ridge to the west with a N25°E strike and a downdrop to the east [*Becker et al.*, 2000]. The volumetric fluid flux through the Baby Bare outcrop is 4–13 L/s [*Thomson et al.*, 1995; *Mottl et al.*, 1998]. Fluid recharge supporting this flow is inferred to occur at Grizzly Bare outcrop 52 km to the south, based on spring, pore fluid, and borehole fluid chemistry, as well as consideration of driving forces and sediment physical properties that preclude the possibility that Baby Bare recharge occurs through surrounding sediments [*Wheat et al.*, 2000, 2002; *Fisher et al.*, 2003a]. Thermal and pore water chemical data presented in this study also show no evidence for recharge through the outcrop itself. Baby Bare springs were marked with numbered plastic and syntactic foam markers tethered to a weight and this numbering convention is followed here. Spring temperatures were 22.9°C (Marker 23), 24.5°C (Marker 30), and 25.0°C (Markers 15 and 17). On the basis of previous results that are consistent with vigorous fluid circulation within upper basaltic basement in this area, measured thermal gradients near the sediment-basement interface, and measured temperatures within basement only kilometers from Baby Bare [*Davis et al.*, 1997a; *Fisher et al.*, 1997, 2003a; *Davis and Becker*, 2002; *Becker and Davis*, 2003], we surmise that the spring fluids from Baby Bare have cooled from 64°C during ascent. We use a 64°C formation fluid temperature within upper basement in the calculations that follow.

[7] Except for the spring at Marker 17, hydrothermally altered seawater flows from basalt through a veneer of sediment (<0.7 m thick) [*Wheat et al.*, 2002]. The spring at Marker 17 flowed through a 0.7-m-deep circular hole in the sediment formed by gravity coring in 1992, which removed the sediment section and allowed hydrothermal fluid to vent directly from basement to the ocean without the influence of local sedimentary diagenetic reac-

tions [*Wheat and Mottl*, 2000; *Wheat et al.*, 2002; *McManus et al.*, 2002]. Additional "springs" were generated when push cores were taken from *Alvin* that removed 20–30 cm of sediment, exposing basalt.

3. Methods

3.1. Outcrop Thermal and Fluid Flow Measurements

[8] One hundred seven thermal gradients were measured using three different thermal probes during thirteen dives with the submersible *Alvin*. Measurements were taken on and around Baby Bare but were most commonly made near areas of fluid venting. Each probe was inserted using the submersible manipulator and the depth of penetration was gauged with marks on the probe. We used a 60-cm-long five-thermistor probe with thermistors at 5, 15, 25, 35, and 45 cm from the tip during the first dive. After penetration into the sediment the probe was released from the manipulator and temperatures were recorded for 5 to 10 min, about the time required for the temperatures to stabilize. A malfunction did not allow us to make in situ measurements of thermal conductivity. This probe was damaged beyond repair on the second dive. On the third dive we used a low-temperature probe with a single thermistor at its tip. This probe was inserted to a depth of 10 cm. After 5 min a temperature was recorded and the probe was inserted another 10 cm. This procedure was repeated until the final temperature was recorded at a depth of 40 cm below the sediment surface. For the remaining dives we used a 55-cm-long probe with thermistors mounted 4, 14, and 24 cm from the tip, and operations followed those of the first dive.

[9] Two additional tools were deployed, one to monitor effluent temperature and the other to estimate volumetric fluid fluxes from individual springs. Effluent temperatures were monitored using self-contained temperature recorders. These recorders were placed on the basaltic outcrop near Marker 15 and in the gravity core hole at Marker 17. Each recorder was deployed for several days and a measurement was recorded every 0.5 hours. Volumetric fluxes from individual springs were determined by placing an inverted PVC funnel over the spring. Spring waters entered the bottom of the funnel (804 cm^2) and exited at the top (3.98 cm^2) where we positioned a 20-cm-long rod with 5-cm demarcations. Flow velocities were estimated from visual observations of the rising plumes.

3.2. Water Column Thermal and Radon Anomalies

[10] Six conductivity-temperature-pressure-nephelometer (CTD-N) hydrocasts were conducted within a 0.8 km radius of the summit of Baby Bare to determine thermal anomalies and to provide water for chemical analyses. Water sampling focused on the lower 200 m of the water column because previous hydrocasts confirmed the presence of thermal and chemical anomalies within this interval [*Wheat et al.*, 1997]. Seawater samples were collected within this interval with some samples only a few meters above the seafloor to provide a measure of diagenetic (nonhydrothermal) inputs. Seawater samples were taken directly from the spigot of acid-rinsed 30-L niskin bottles into evacuated glass carboys for ^{222}Rn analyses. This water was then stripped, and the radon was transferred to a scintillation counting system [e.g., *Kadko and Moore*, 1988].

[11] Our approach for estimating the advective power output from Baby Bare using ^{222}Rn, which is a chemically inert radioactive gas with a half-life of 3.85 days, data from the nonbuoyant plume is based on the approach used by *Rosenberg et al.* [1988] and *Gendron et al.* [1994]. This technique works well with submarine hydrothermal systems because the concentration of radon in the venting fluids is several orders of magnitude greater than that in bottom seawater [e.g., *Dymond et al.*, 1983; *Kadko and Moore*, 1988]. However, radon in excess of the local background level (~27 dpm/100 L) can be generated within bottom sediments and subsequently mixed into the overlying water through bottom turbulent mixing, potentially competing with radon injected directly into the effluent hydrothermal plume at springs. If the bottom source does not reach the height of the hydrothermal plume, which is the case near Baby Bare, then the venting source of radon is ascertained unambiguously. Here we estimate the standing crop of excess radon in the effluent plume, which is assumed to be at steady state. From the 3.85-day half-life of ^{222}Rn, this standing crop is converted into a chemical or mass flux of radon from the springs into the overlying plume. An advective power output is estimated from the measured radon/heat ratio of spring fluids.

3.3. Calculating Heat Flow Values From Sediment Thermal Gradients

[12] Most of the temperature data were reduced using the methods described by *Bullard* [1954] and

Villinger and Davis [1987] and a constant thermal conductivity of 0.89 (±0.09 s.d.) W m^{-1} $°C^{-1}$, which was determined from needle-probe measurements in the upper meter of cores recovered nearby during a later expedition [*Fisher et al.*, 2003a]. The heat flow probe is idealized as an infinitely long "line source" for frictional heating associated with insertion. Observations are extrapolated to equilibrium temperatures by fitting them to an analytical temperature versus time solution for the specified thermal conductivity. Temperature data for several of the penetrations did not fit the transient cooling model because of additional settling or movement after probe penetration. For these penetrations we estimated equilibrium temperatures by extrapolating the short temperature record to infinite time, minimizing the variance near the end of the temperature record (Table 1). In contrast, temperature was not recorded continuously for the eight penetrations using the second, single-thermistor temperature probe. For these measurements we used the last recorded values before the probe was moved to a new depth (Table 1).

3.4. Estimating Heat Flow Components

[13] The sediment drape across Baby Bare outcrop was considered to behave as a boundary layer having fixed upper and lower temperatures. Under purely conductive conditions, heat flow through the sediment is inversely proportional to layer thickness. Fluid seepage perturbs the temperature-depth profile across the sediment, but total heat flow (q_{tot}) is still entirely conductive across the upper boundary [*Bredehoeft and Papadopulos*, 1965]. This idealization applies everywhere except where focused springs occur, since springs allow fluid with a temperature greater than that of bottom seawater to penetrate the seafloor. Focused fluid flow out of springs rises adiabatically at the scales we are considering, and results in heat transport that is entirely advective. But everywhere else, the total heat flow can be partitioned into a conductive component (q_{con}) and an advective component (q_{adv}). Making this distinction allows us to assess the relative importance of heat loss mechanisms from the entire outcrop and the volumetric fluid flux. Given the volumetric flux, chemical fluxes can be estimated from the ratio of chemical/thermal anomalies.

[14] Each set of thermal probe data was examined to determine whether the thermal gradient was linear or nonlinear. A gradient was considered to be nonlinear only if systematic curvature could not be explained by reasonable variations in sediment thermal conductivity (up to two standard deviations from the mean). Nonlinear thermal gradients (10% of the data) were analyzed using an analytical model of one-dimensional, steady state advection and diffusion through a layer having fixed upper and lower temperatures [*Bredehoeft and Papadopulos*, 1965]. The lower boundary of the layer was placed at the depth of the deepest temperature measurement, and the fluid specific discharge or seepage speed (volume flux/area, also known as the "Darcy velocity") was estimated using a least squares, best-fit approach. This method is sensitive only to seepage speeds exceeding a minimum value, v_z, defined by

$$v_z = 0.5\lambda / c_o \rho_o L, \quad (1)$$

where v_z is the limit of detectable vertical fluid seepage, λ is the thermal conductivity, c_o is the heat capacity of seawater (4200 J Kg^{-1} $°C^{-1}$), ρ_o is the density of seawater (1024 kg m^{-3}), and L is the length of the probe (m). For a 0.5-m-long probe the detection limit is ~6.5 m yr^{-1}. For these measurements q_{adv} is a minimum, since we can not extrapolate downward to estimate the depth to the 64°C isotherm (which we believe to be the base of the boundary layer, see discussion below).

[15] If a measured thermal gradient was linear (meaning that the seepage rate was less than ~6.5 m yr^{-1}), we examined geochemical data collected from co-located push cores. About 70% of all heat flow measurements had co-located push cores. Geochemical data were fit to an advection-diffusion model very similar to that used for assessing curvature in thermal data to estimate v_z. Because the chemical diffusivity for solutes is about three orders of magnitude smaller than thermal diffusivity, chemical data are much more sensitive to fluid flow (Figure 2) [e.g., *Wheat and McDuff*, 1995]. At upward fluid seepage rates >2 m yr^{-1}, solute concentrations within the upper 0.5 m of sediment are practically constant, and there are extreme gradients within the uppermost centimeter of sediment. These extreme gradients are difficult to measure because they are altered by diffusion and physical disturbance during core retrieval and processing [*Wheat and McDuff*, 1995]. The lower limit on seepage detection using geochemical data from the upper 0.5 m of sediment is ~0.005 m yr^{-1}.

[16] After chemical data were used to estimate v_z, this value was used with the advection-conduction model described earlier to estimate the depth to the

Table 1. Locations of Heat Flow Measurements, Markers, and Hydrocasts and Calculated Parameters Based on the Thermal Data and an Assessment of Seepage Speeds

Station	Latitude 47°N, min	Longitude 127°W, min	Depth, m	Number of Temp. Meas.	Total Heat Flow, W/m^2	Maximum Conductive Heat Flow, W/m^2	Depth to 64°C, m	ΔP Calculated, kPa
2966-1	42.854	47.162	2660	5	1.02	1.00	55	28
2966-2	42.849	47.102	2660	4	3.80	3.15	18	61
2966-3	42.618	47.159	2605	4	8.90	8.62	6.4	2.7
2966-4	42.593	47.224	2614	5	2.49	2.45	22	6.2
2966-5	42.574	46.984	2660	5	1.29	1.27	44	17
2969-1	42.588	47.525	2660	4[a]	0.80	0.79	70	23
2969-2	42.599	47.433	2660	4[a]	1.23	1.13	49	110
2969-3	42.607	47.356	2652	4[a]	4.89			
2969-4	42.605	47.344	2650	4[a]	2.16	1.53	36	300
2969-5	42.601	47.308	2631	4[a]	2.27	2.05	27	57
2969-6	42.606	47.258	2616	4[a]	2.99	2.78	20	28
2969-8	42.614	47.146	2611	4[a]	17.9	14.4	3.8	1.4
2969-9	42.592	47.082	2644	4[a]	2.26	2.21	25	12
2970-1	42.578	47.228	2638	3	4.18	3.95	14	13
2970-2	42.604	47.24	2611	3	9.21	8.84	6.2	3.3
2970-3	42.591	47.182	2606	3	66.3	65.2	0.85	0.1
2970-5	42.591	47.173	2602	3[b]	14.4	13.6	4.1	2.6
2970-6	42.601	47.16	2599	3	18.9	15.4	3.6	8.2
2971-1	42.773	47.213	2661	3	1.37	1.27	44	85
2971-2	42.784	47.198	2661	3	4.57	4.36	13	10
2971-3	42.746	47.192	2641	3[b]	0.55	0.54	100	12
2971-4	42.717	47.188	2626	3	0.39	0.39	140	46
2971-5	42.635	47.22	2612	3	1.77	0.50	110	
2971-6	42.554	47.22	2641	3	12.2	11.3	4.9	4.6
2971-7	42.558	47.208	2636	3	425	51		4.7
2971-8	42.558	47.199	2628	3	3.37	0.31	18	24
2971-9	42.584	47.179	2608	3	11.2	10.8	5.1	2.4
2972-1	42.59	47.182	2605	3	72.7	72.1	0.77	0.0
2972-2	42.601	47.173	2599	3	14.3	13.7	4.0	2.1
2973-1	42.509	47.116	2661	3	2.67	2.52	22	25
2973-2	42.52	47.122	2649	3	1.21	1.15	48	70
2973-3	42.529	47.127	2634	3	1.08	0.84	66	
2973-4	42.598	47.182	2604	3	190	55		3.0
2973-5	42.605	47.173	2596	3	6.24	5.94	9.3	7.0
2974-1	42.73	47.097	2634	2	2.00	1.78	31	78
2974-2	42.718	47.11	2624	3	0.65	0.41	130	
2974-3	42.7	47.102	2616	3	1.34	1.12	49	230
2974-4	42.685	47.098	2607	3	9.40	9.19	6	1.7
2974-5	42.607	47.158	2601	3	32.6	13.9		2.8
2974-6	42.601	47.16	2600	3	154	34		4.4
2974-7	42.601	47.177	2602	3	26.0	25.3	2.2	0.6
2974-8	42.601	47.179	2602	3	180	43		2.1
2974-9	42.6	47.179	2603	3	25.4	24.4	2.3	0.9
2974-11	42.59	47.186	2611	2	41.9	40.9	1.4	0.3
2975-2	42.612	47.165	2604	3	3.26	3.22	17	3.9
2975-3	42.571	47.006	2594	3	2.40	2.39	23	1.6
2975-4	42.579	47.063	2661	3	2.49	2.47	22	2.9
2975-5	42.569	47.117	2629	3	5.33	4.23	13	51
2975-6	42.582	47.155	2610	3	13.1	12.3	4.5	3.6
2975-7	42.589	47.169	2602	3	4.98	3.92	14	59
2976-1	42.731	47.088	2635	3	4.67	4.42	13	11
2976-2	42.747	47.084	2629	3	1.94	1.69	33	100
2976-3	42.629	47.119	2615	3	5.67	3.90	14	94
2976-4	42.621	47.129	2607	3	13.5	12.6	4.4	3.5
2976-5	42.596	47.182	2603	3	70.8	69.7	0.79	0.1
2976-6	42.556	47.194	2624	3	4.22	3.89	14	19
2977-1	42.589	47.185	2606	2	19.8	19.6	2.8	0.3
2977-2	42.592	47.181	2604	3	22.1	21.7	2.5	0.5
2977-3	42.592	47.177	2602	3	7.98	7.56	7.3	5.4

Table 1. (continued)

Station	Latitude 47°N, min	Longitude 127°W, min	Depth, m	Number of Temp. Meas.	Total Heat Flow, W/m^2	Maximum Conductive Heat Flow, W/m^2	Depth to 64°C, m	ΔP Calculated, kPa
2977-4	42.592	47.167	2599	3	12.2	11.5	4.8	3.5
2977-5	42.598	47.186	2606	3	7.16	7.08	7.8	1.2
2977-6	42.591	47.185	2607	3	207	52		2.0
2977-7	42.59	47.183	2607	3	18.3	17.8	3.1	0.7
2977-8	42.583	47.179	2606	2[b]	6.21	3.42	16	190
2977-9	42.601	47.186	2603	3	9.60	8.75	6.3	7.7
2977-10	42.601	47.181	2601	3	489	68		3.7
2977-11	42.604	47.177	2599	3	21.3	20.2	2.7	1.4
2978-3	42.475	47.243	2647	3[b]	0.78	0.77	72	26
2978-4	42.514	47.249	2645	3	1.55	1.49	37	35
2978-5	42.537	47.215	2643	3	3.46	3.07	18	40
2978-6	42.544	47.201	2638	2	2.56			
2978-7	42.575	47.194	2622	3	29.4	28.1	2.0	0.8
2979-1	42.704	47.232	2639	3	0.54	0.54	100	19
2979-2	42.598	47.182	2603	3	410	86		2.6
2979-3	42.505	47.469	2661	3	1.66	1.62	34	16
2979-4	42.532	47.394	2659	3	2.22	2.08	27	36
2979-5	42.553	47.348	2646	3	1.36	1.33	41	21
2979-6	42.572	47.28	2642	3	2.60	2.38	23	40
2979-7	42.574	47.274	2629	3	6.72	6.68	8.3	0.9
2979-8	42.596	47.216	2621	3	8.11	3.25	17	340
2979-9	42.596	47.196	2611	3	5.79	3.28	17	190
2979-10	42.597	47.189	2607	3	7.76	6.67	8.3	18
2979-11	42.596	47.182	2603	3	383	53		5.5
2979-12	42.596	47.179	2601	3	11.5	9.3	6.0	17
2980-2	42.736	47.402	2662	3	0.58	0.55	100	23
2980-3	42.731	47.343	2661	3	0.75	0.72	77	80
2980-4	42.699	47.287	2655	3	2.29	1.26	44	
2980-5	42.67	47.287	2645	3	0.59	0.51	110	
2980-6	42.65	47.267	2631	3	1.30	1.17	47	120
2980-7	42.643	47.228	2616	3	1.80	1.49	37	164
2981-1	42.479	47.405	2659	3	1.19	1.10	50	93
2981-2	42.512	47.362	2647	3	0.91	0.89	62	39
2981-3	42.541	47.299	2644	3	1.83	1.78	31	16
2981-4	42.553	47.257	2642	3	1.33	1.24	45	84
2981-5	42.555	47.22	2640	3	18.0	11.5		1.4
2981-6	42.569	47.203	2627	3[b]	18.7	18.7	3.0	0.0
2981-7	42.586	47.188	2610	3	57.6	31.7		2.0
Marker 15	42.590	47.182						
Marker 17	42.601	47.178						
Marker 20	42.555	47.221						
Marker 23	42.598	47.182						
Marker 28	42.615	47.158						
Marker 29	42.574	47.194						
Marker 30	42.597	47.182						
Cast 1	42.515	46.833						
Cast 3	42.679	47.081						
Cast 9	42.866	47.164						
Cast 12	42.641	47.103						

[a] Determined from the last recorded temperature.
[b] Determined using the inverse time extrapolated to infinite time.

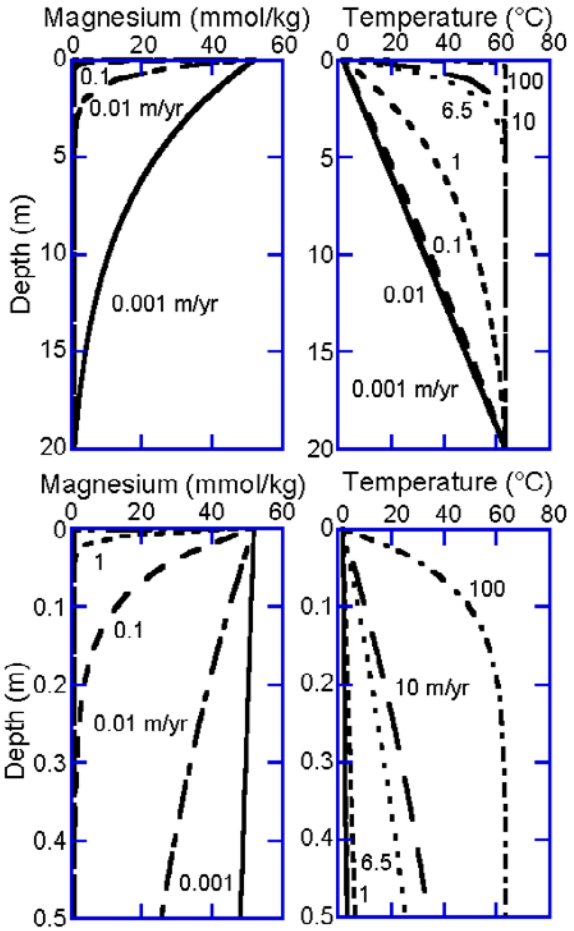

Figure 2. Calculated pore water magnesium and temperature profiles for various upward seepage speeds (m yr^{-1}). A 50-cm-long magnesium profile provides a good measure of the seepage velocity in the range of 0.001 to several meters per year. A 50-cm-long temperature profile is useful for determining seepage speeds faster than about 6.5 cm yr^{-1}. Slower seepage speeds can be determined with longer profiles. Boundary conditions are $Mg_{(z=0\ m)}$ = 52 mmol kg^{-1}; $Mg_{(z=20\ m)}$ = 1 mmol kg^{-1}; $T_{(z=0\ m)}$ = 1.7°C; $T_{(z=20\ m)}$ = 63.5°C. The diffusion coefficient for Mg is 3.82 × 10^{-6} cm^2 s^{-1} based on the diffusion coefficient at infinite dilution at 2°C [*Li and Gregory*, 1974]. The diffusion coefficient was adjusted to consider a porosity of 0.85 and a formation factor of 2. The thermal diffusivity is 0.89 W $°C^{-1}$ m^{-1}.

64°C isotherm, $z_{64°C}$. We had to determine the pore water velocity independently because it is otherwise not possible to downward continue thermal data with confidence. For example, given appropriate sediment properties and a 0.5 m-long probe, the calculated thermal gradient with a temperature of 64°C at a depth of 3.3 m and no fluid flow is the same as that with a temperature of 64°C at a depth of 20 m with an upward seepage rate of 2 m yr^{-1}

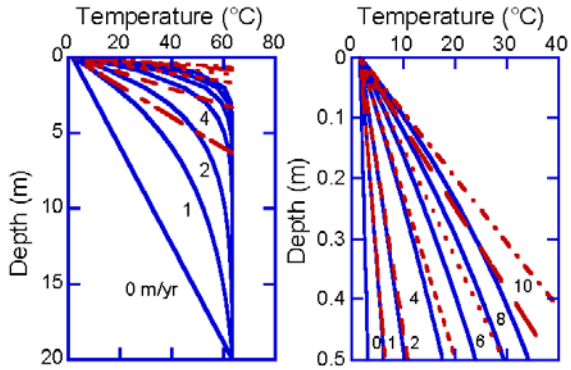

Figure 3. Calculated temperature-depth profiles that illustrate the nonunique calculation for heat flow. For example, profiles calculated using boundary conditions of $T_{z=0\ m}$ = 1.7°C and $T_{z=20\ m}$ = 63.5°C for given upward seepage velocities (solid lines) have similar temperature gradients near the sediment-water interface as conductive (dashed) profiles. Note the different depth scales.

(Figure 3). We consider $z_{64°C}$ to be the base of the boundary layer, allowing calculation of heat flow components. q_{con} across the layer is calculated from $z_{64°C}$ and a temperature difference of 62.3°C (relative to bottom water). q_{con} is subtracted from q_{tot} (determined with the short probe) to estimate q_{adv}.

[17] The final case is one in which the thermal gradient is linear and there are no co-located chemical data (20% of the data). In this case, q_{tot}

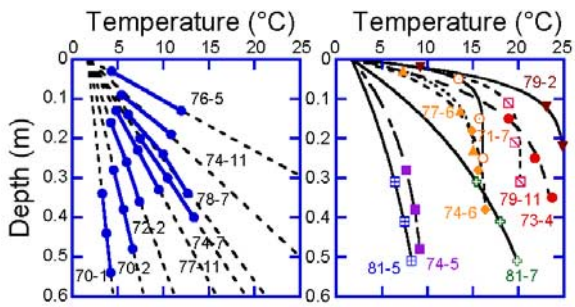

Figure 4. Selected temperature data plotted as a function of depth for both conductive and conductive-advective profiles. "Conductive" profiles may include an advective component. For these profiles the seepage speed is sufficiently slow such that the speed cannot be determined from the heat flow data alone. Solid lines connect data, and dashed lines are calculated profiles using speeds determined from systematic variations in pore water chemical profiles and a thermal diffusivity of 0.89 W $°C^{-1}$ m^{-1}. If flow is faster than about 6.5 m yr^{-1}, then we used the seepage speed based on thermal data to calculated heat flow. Numbers identify particular *Alvin* dives (add 2900) and penetration number.

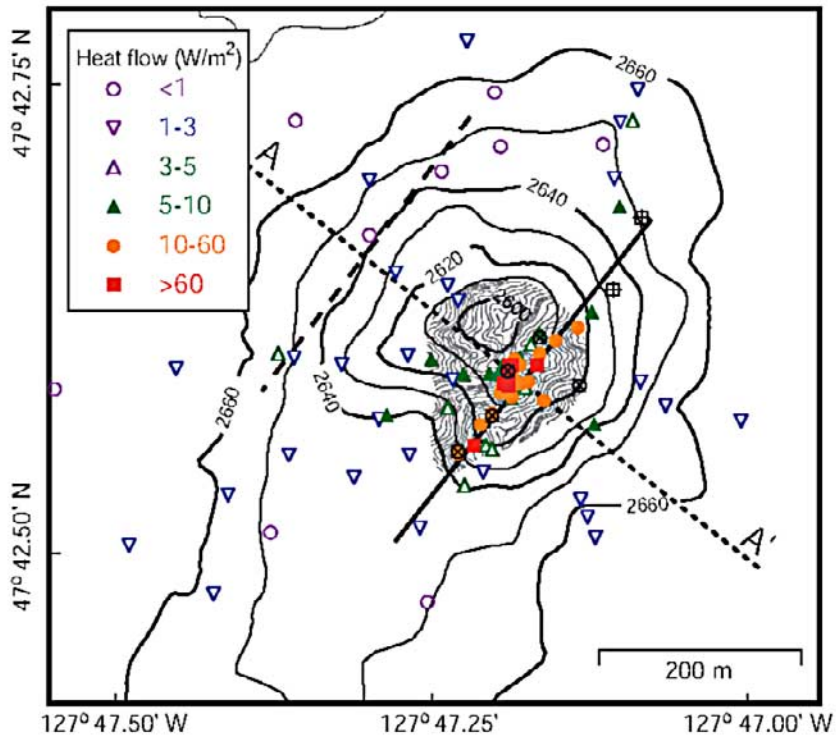

Figure 5. Location of total heat flow measurements, markers, and hydrocasts. The solid line defines the main fault on which the springs were located. Markers 15, 17, and 23 are shown at the intersection of A-A′ and the line that defines the main fault (Table 1). The dashed line is parallel to this solid line and bisects a fault and a heat flow high to the west (some of the high values are north of the area that is shown). The transect A-A′ is shown in Figures 7 and 10. The shaded area near the summit defines an area within which sediments are <1 m thick. Markers are shown as circles with a plus sign. Hydrocasts are shown as squares with a plus sign (Table 1).

was determined from probe data, as described above, and relative partitioning into advective and conductive components was estimated through comparison with sites having similar q_{tot} with co-located geochemical data.

[18] We highlight some of the temperature profiles and calculations in Figure 4 to show the range of thermal data that was collected and the goodness of model fits to these data.

4. Results and Discussion

4.1. Power Output From Thermal Measurements

[19] The lowest calculated heat flow value in this study is 0.39 W m^{-2}, somewhat greater than the predicted conductive value of 0.27 W m^{-2} for 3.5-Myr-old lithosphere [*Davis et al.*, 1997b] (Table 1). Eight measurements yielded heat flow values greater than 150 W m^{-2} and the highest was 490 W m^{-2}. The distribution of these heat flow measurements is shown in Figure 5, illustrating three distinguishing features:

[20] 1. The highest heat flow values are confined to the immediate vicinity (15-m-wide band) of a northeast trending fault near the summit of the outcrop where we observed shimmering water, springs, and communities of thysirid clams [*Becker et al.*, 2000]. Fluid and heat fluxes along this fault are spatially highly variable. For example, stations that are 5 m apart (2979-2 and 2977-5) have total heat flow values of 7.2 and 410 W m^{-2}, and upward seepage speeds of 0.02 m y^{-1} and 130 m yr^{-1}, respectively.

[21] 2. A second heat flow high is observed west of the main fault along another northeast-trending fault with a relief of 2 m and no evidence for springs [*Becker et al.*, 2000]. The highest heat flow value along this fault is 9.2 W m^{-2} (other high values are north of the plotted area in Figure 5). This high heat flow is consistent with warm water being present at a shallow depth below the sea-floor, but only slow seepage through the sediment

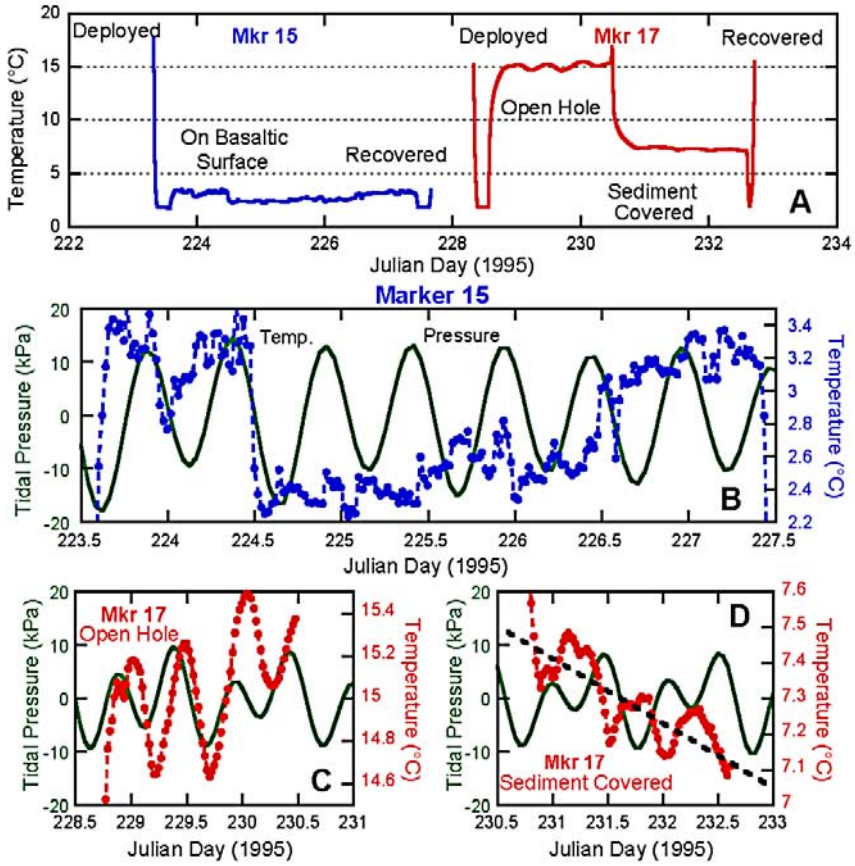

Figure 6. Temperature record from two self-contained temperature recorders. (a) One was positioned on basaltic outcrop near Marker 15 and (b) was exposed to bottom currents. (c) The other recorder was deployed in the open hole at Marker 17. (d) Two days later some sediment poured into the hole when the submersible *Alvin* was deploying an instrument. The effect of this sediment was to restrict fluid flow, resulting in a lower temperature and changing the phase in the record relative to the tidal signal. Tidal data were calculated by Harold Mofjeld (PMEL, Seattle, Washington).

occurs in this area. Here the sediment is generally thicker than along the main fault, illustrating the capability of sediment to slow the egress of formation fluid from basaltic basement.

[22] 3. Heat flow is uniformly much higher over much of the outcrop than through the surrounding area. We refer to this feature later as the ''broad heat flow high''.

[23] In places the sediment was too thin to use the heat flow probe. In such places we determined the local heat flux by placing the inverted funnel over individual springs. For example, formation fluids at Marker 17 rise through a 7.62-cm-diameter hole left by a gravity core barrel into the larger diameter hole that was made from the weight stand. A temperature of 25.0°C was measured in the upper part of this hole. Considering the diameter of the funnel and an estimated exit speed of 4 to 5 cm s^{-1}, we calculated a volumetric flux of 0.016 to 0.020 L s^{-1}, corresponding to a power output or heat flux of 0.0016 to 0.0019 MW. Unfortunately the seal between the inverted funnel and the seafloor was not complete and about one third of the flow exited from the base of the funnel. Taking into account this additional flow, the power output is 0.0024 to 0.0029 MW. If this power output is uniformly distributed through the 7.62-cm diameter hole left from coring, the calculated heat flow is 34 to 43 W m^{-2} from bare basalt. Similar fluid flows were observed at Marker 15 where the inverted funnel was placed on basalt. The fluid exit speed was ~1 cm s^{-1}, resulting in a calculated power output of 0.00038 MW. Assuming this flow is uniform through basalt under the funnel, the calculated heat flow is 0.48W m^{-2}.

[24] To assess the degree to which changes in tidal pressure or varying bottom water currents may

affect our measurements, we deployed two temperature recorders (Figure 6a). One was placed on bare basalt near Marker 15. The phase relationship between pressure (tidal signal) and temperature is not well defined at Marker 15, but a total temperature variability of about 1.1°C was recorded. This is as large as the average thermal anomaly at this site (Figure 6b), which suggests that any instantaneous measurement of the power output from exposed basalt could be in error by a factor of two. However, even a value twice as great as that calculated above would still be insignificant when compared to nearby measurements within the sediment.

[25] The other temperature recorder was placed in the hole from which fluids vented at Marker 17. This hole collapsed slightly during submersible operations before the recorder was deployed, resulting in a slightly lower temperature (15°C) than that originally measured (25.0°C) (Figure 6c). During the first two days of the deployment the recorder measured temperature maxima at times of falling seafloor pressure, i.e., when the pressure gradient in the sediment immediately surrounding the corehole would have been maximized. The range of the measured thermal anomaly is ~5%, which has a minor effect on the power output calculation above for direct focused venting of spring waters.

[26] Two days after this instrument was deployed the spring was altered further when we deployed a large instrument that caused the surrounding sediment to collapse into the hole. Sediment covered the recorder, and temperatures dropped to 7°C, presumably because of the reduced advective heat transport (Figure 6d). The amplitude of the tidal temperature variations decreased, and the sign of the correlation between temperature and pressure reversed: observed temperature maxima corresponded to tidal pressure minima. The continued decrease in temperature during the two-day period following the disruption is probably related to changes in hydraulic impedance as the sediment responds to periodic loading and unloading. The general trend of the temperature maxima corresponding to the tidal pressure minima is consistent with the ocean overlying a confined basement aquifer that responds elastically to tidal loading (i.e., no phase shift [e.g., *Davis et al.*, 2000]). Thus, during high tide, when the seafloor pressure is highest, the net formation overpressure reaches a minimum, resulting in lower rates of fluid flow and temperatures. If this observation represents the typical condition and the interpretation that the near-seafloor formation-fluid pressure regime in this edifice is dominated by the regional elastic crustal loading response, it implies that the amount of flow from Baby Bare is small relative to the ability of the crustal reservoir to deliver fluid (e.g., high formation capacity and permeability). Semiburied edifices like Baby Bare may provide a good opportunity to monitor regional crustal hydrologic conditions such as the response to plate deformation [e.g., *Davis et al.*, 2001] without the expense of drilling deep boreholes.

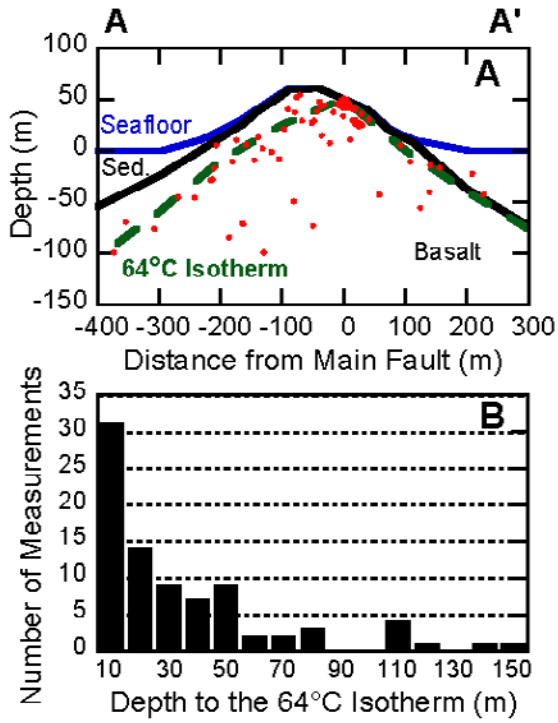

Figure 7. Depth of the calculated 64°C isotherm in reference to the distance from the main fault along the transect A-A′ shown in Figure 5. (a) Depths are calculated from the heat flow data and seepage speeds determined from the chemical data; thus data are limited to areas where seepage speeds are less than several meters per year. The dashed line represents the expected 64°C isotherm, which extends above the turbidite plain. (b) The bar graph indicates the number of measurements in which the calculated depth falls within a particular 10 m bin. The number on the *x* axis represents the deepest extreme for a particular bin. For example, the bin labeled 10 includes the data from 0 to 10 m depth.

[27] We calculate a minimum power output or heat flux of 1.5 MW from Baby Bare by extrapolating our results over the entire feature. Our power output calculation is an order of magnitude greater

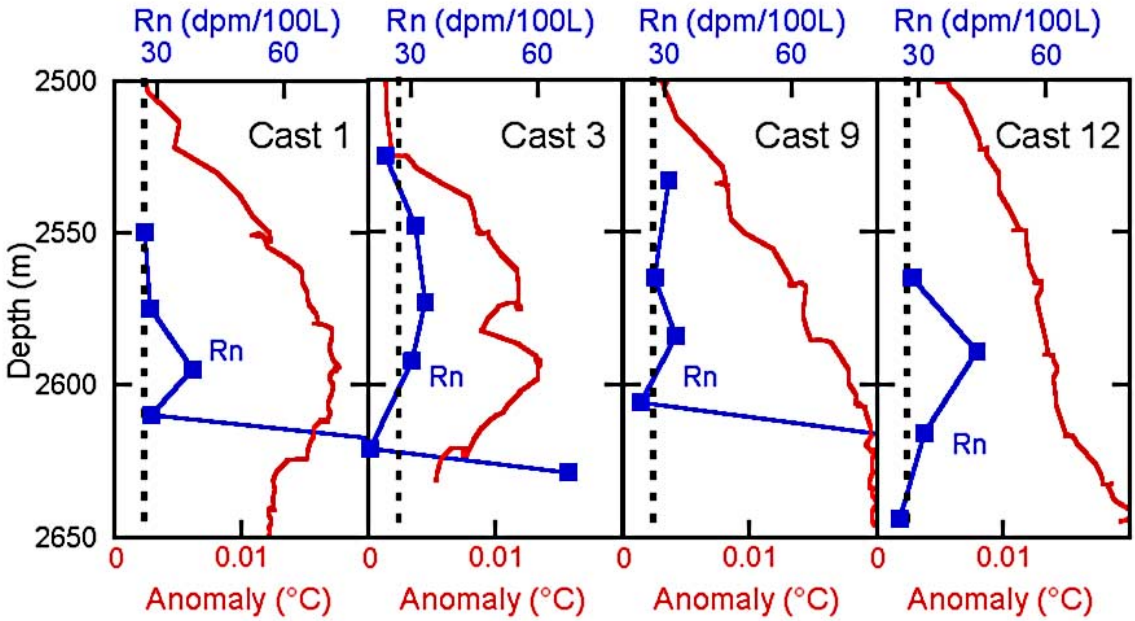

Figure 8. Water column anomalies of ^{222}Ra (squares) and temperature anomaly (solid line). Background ^{222}Ra concentrations are 27 dpm/100L and are shown with a dotted line.

than that predicted for conductive cooling of 3.5-Myr-old crust (0.14 MW for a 0.5 km^2 area). About one-third of this power output comes from less than 15% of the surface area and ~1.3 MW (84%) of the power output is conductive. Our power output is consistent with preliminary estimates of 2 to 3 MW reported by *Mottl et al.* [1998], who consider a broader areal extent. If we expand our analysis to include those measurements made during earlier expeditions [e.g., *Davis et al.*, 1997b], the power output for a 1.65 km^2 area is 2.2 MW. Of this additional 0.64 MW, 0.45 MW is the power output associated with typical crustal heat loss for the area. Our calculated power output for this larger areal extent is at the lower end of the range of 2 to 24 MW based on models of thermal anomalies in the overlying water column [*Thomson et al.*, 1995].

[28] Calculated depths to the 64°C isotherm ($z_{64°C}$) range from a few meters near and along the main fault to ~140 m (Figure 7a) (Table 1). If we exclude the 29 measurements that were collected along the main fault where $z_{64°C}$ is <10 m (average of 4.3 m), then the average value of $z_{64°C}$ is 43 m. A majority of these 55 calculated depths for $z_{64°C}$ are within the range of 10 to 50 m; only seven values are greater than 80 m (Figure 7b). This bimodal distribution of isotherm depths results, in part, from our sampling scheme which was skewed toward areas of possible venting. Nevertheless this analysis indicates that $z_{64°C}$ commonly lies above the surrounding seafloor (Figure 7a).

[29] Even though we visualize basaltic outcrops as permeable crustal ventilators, faults or highly connected permeable paths that have an expression at the seafloor appear to strongly influence fluid and associated fluxes. This finding illustrates that, even within rocks having high "background" permeability, fluids tend to follow the most permeable pathways. It is interesting to note that along the western fault the calculated 64°C isotherm ($z_{64°C}$) is within ~13 m of the seafloor. This suggests that only a thin layer of sediment (with or without surficial altered mineralized basalt) is required to preclude the formation of warm springs, but the sediment layer is thin enough to allow some pore water seepage to occur. Even thin sediment layers can "cap" highly permeable basaltic crust and limit fluid, heat, and chemical advection. For example, we generated springs by removing only 20 to 30 cm of sediment while taking push cores along the main fault.

4.2. Power Output From Water Column Measurements

[30] Individual profiles of ^{222}Rn and potential temperature anomaly (deviation of temperature from the potential temperature-density relationship of ambient bottom water) are shown in Figure 8. For

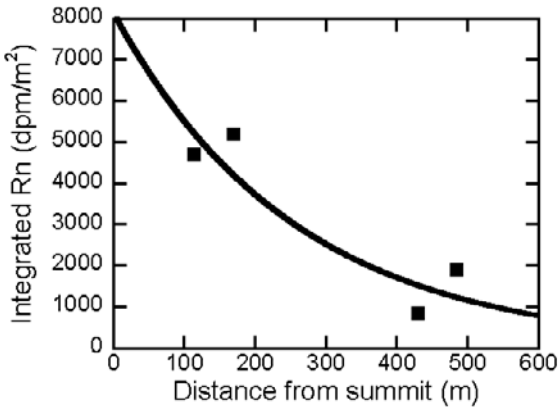

Figure 9. The integrated ^{222}Rn anomaly as a function of distance from the summit. The solid line is the best fit to the data assuming an exponential decay away from the summit.

hydrocasts 1, 3, 9 and 12 the bottom sediment source lies well below the plume at ~2590 m depth. This source is particularly well defined by ^{222}Rn and temperature anomalies from hydrocasts 1 and 3. The integrated excess ^{222}Rn in the effluent plume for these four hydrocasts ranges from 850 to 5200 dpm m^{-2} with the smaller values being farther from the summit and springs (Figure 9). The observed decrease in radon with distance away from the springs is relatively well fit by the function:

$$Rn = 8150\exp(-0.0039\,x), \qquad (2)$$

where Rn is the integrated excess of ^{222}Rn (dpm m^{-2}) and x is distance (m) from the summit of Baby Bare. Using this function we calculate the excess radon by integrating symmetrically around the summit, resulting in a standing crop of radon of 4.9×10^9dpm. The advective power output is calculated from the measured radon/heat anomaly in spring fluids. The maximum spring temperature was 25.0°C and the maximum ^{222}Rn concentration was 2650 dpm L^{-1} [*Mottl et al.*, 1998], yielding a radon/temperature ratio of 0.11 dpm g^{-1} °C^{-1} and a radon/heat ratio of 212 atoms j^{-1}. Dividing the standing crop (4.9×10^9dpm) by the radon/heat ratio of the venting fluid results in an advective power output from Baby Bare of 0.39 MW, which is consistent with the difference in the total power output (1.52 MW) and the conductive power output (1.28 MW) derived earlier.

4.3. Reservoir Structure

[31] Two-dimensional models for the warm hydrothermal reservoir that underlies seafloor springs have been developed for other settings. These models have focused on either a pipe-like permeable path suitable for high temperature hydrothermal systems on mid-ocean ridges [e.g., *Sleep and Wolery*, 1978] or a well mixed basaltic reservoir that simulates a basaltic mass above a normally flat basaltic plain [*Hardee and Larson*, 1980; *Stein et al.*, 1998]. Some of the questions that these models

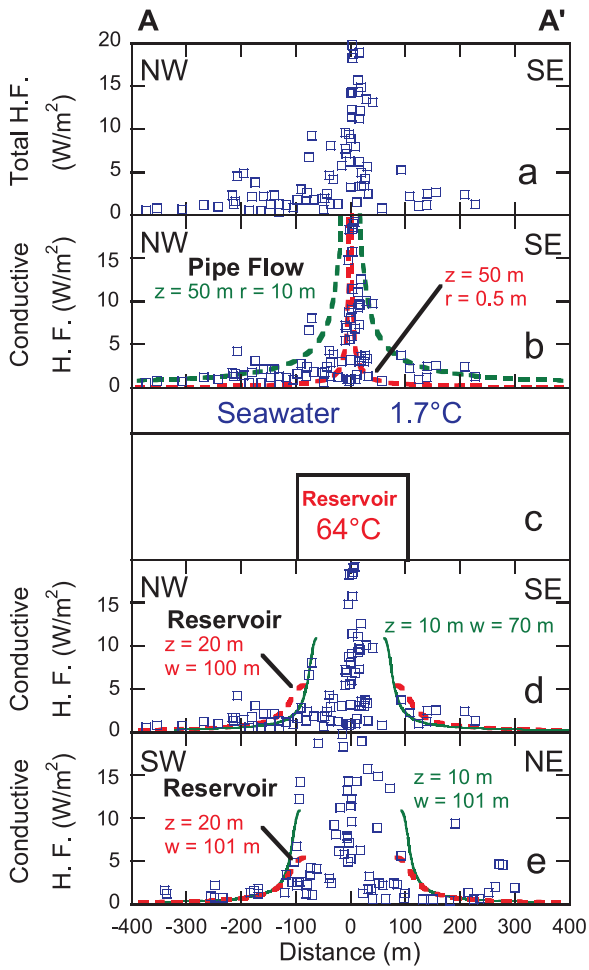

Figure 10. Total and conductive heat flow relative to the distance from a fixed plain defined by the main fault with several modeled profiles. All of the heat flow values greater than 20 W m^{-2} are not shown but center around the main fault. Calculations from two models are shown with respect to the conductive component of the heat flow. These models consider pipe flow (Figure 10b) and a "top hat" mixed reservoir (Figures 10c, 10d, and 10e). A schematic for the "top hat" model is shown in Figure 10c. Calculations of this model are provided for transects perpendicular to the main fault (NW to SE; A-A′ in Figure 5) (Figure 10d) and along the main fault centered at Marker 23 (SW-NE) (Figure 10e). The data are best fit to simulations with a reservoir that is 70 m wide perpendicular to strike and 100 m wide along strike, which is the distance between Markers 20 and 17.

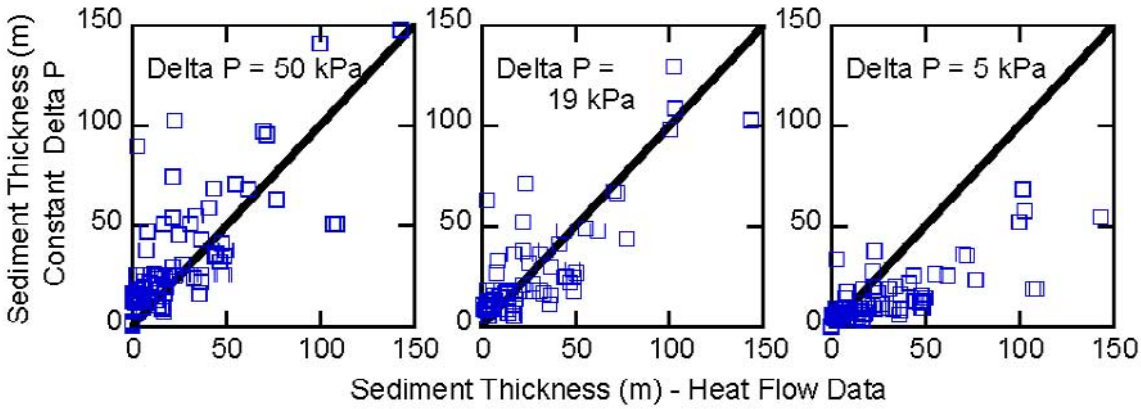

Figure 11. Sediment thickness determined from the heat flow data are plotted against the sediment thickness calculated assuming a constant ΔP, an impedance function, and the seepage speeds calculated from pore water chemical data. Three examples are shown that bracket the best fit to the data which results from using a ΔP of 19 kPa.

attempt to constrain include: (1) is fluid venting consistent with the mining of heat from depth via permeable faults and pathways?; (2) does fluid venting mine heat from a well-mixed shallow reservoir?; and (3) what is the geometry of isotherms within the crust? In the following analysis we present two models and show that a well-mixed, shallow reservoir with an irregular shape, combined with focused pipe-like flow through faults above the reservoir, is consistent with thermal observations. For purposes of comparison, idealized cross-sections are drawn through Baby Bare outcrop along the main fault and perpendicular this feature (Figure 5), and heat flow values are projected onto these profiles (Figure 10).

[32] High heat flow values in the vicinity of the main fault are well explained by a vertical, focused flow. For this calculation we used the solution of *Sleep and Wolery* [1978] for a pipe-like source in a two dimensional radial system. We assume a thermal conductivity of 0.89 W m^{-1} K^{-1}, a formation temperature of 64°C, a depth to the 64°C isotherm of 50 m (top of the shallow fluid reservoir), and pipe radii of 0.5 and 10 m. The narrow width of the observed thermal anomaly suggests a narrow feeder zone, but elevated heat flow over the remainder of the edifice requires a shallower depth to the 64°C reservoir (Figure 10b).

[33] To illustrate how a shallow reservoir can generate a broad heat flow high surrounded by low background values, we present a two-dimensional model that has a reservoir with a flat top, vertical sides, and extends to an infinite depth at its base [*Hardee and Larson*, 1980; *Stein et al.*, 1998] (Figure 10c). Two examples compare results of calculations based on this model to heat flow values. Figure 10d shows heat flow with distance perpendicular to the main fault. Figure 10e shows heat flow along strike of the main fault centered on the location of Marker 23. For each case, we show two combinations of reservoir widths and depths to the top of the 64°C isotherm that are consistent with the regional data; ~0.16 W m^{-2} at 500 m and ~0.08 W m^{-2} at 1000 m. The best fit of model simulations to the data requires a shallow reservoir with the depth to the top of the reservoir ($z_{64°C}$) being <20 m. Given a $z_{64°C}$ = 10 m, a reservoir that is 70 m wide (NW–SE) and 100 m long (NE–SW) is consistent with the data. This size is reasonable considering the geometry of the outcrop and the distance of 101 m between Markers 20 and 17, which define the range of spring locations along the main fault. This model fails to account for local variability in heat flow, including many relatively low values, which we interpret to indicate that the top of the reservoir is actually irregular, shallower in some areas and deeper in others, with a complex pattern of conduits and faults that feed the springs. This pattern is not a result from local, minor recharge, because co-registered pore water profiles indicate upward seepage or no seepage at all.

4.4. Driving Force for Circulation

[34] Fluid driving forces in basement are calculated using Darcy's law, the viscosity of water, calculated pore fluid seepage speeds, and estimated hydraulic impedance. The hydraulic impedance of the sedi-

ment layer is calculated from $z_{64°C}$ and the empirical relationship for the integrated impedance as a function of depth (z) for a hemipelagic sediment section ($I = 1.409 \times 10^{13} \times z^{2.323}$ [*Giambalvo et al.*, 2000]). Calculated pressure differentials range from 0 to 350 kPa (Table 1); this large range results from uncertainties in the estimated $z_{64°C}$, seepage velocity, and impedance values. The impedance function that we used does not account for authigenic clay minerals, which were evident in most of the cores, and basalt, which has an unconfined permeability structure. Calculated driving pressures are systematically lower near the main fault and higher on the edges of the outcrop.

[35] Excess fluid pressures, originating at the base of the boundary layer, $z_{64°C}$, also correspond to a set of temperature-depth profiles. We compare calculations of $z_{64°C}$ based on a specific driving pressure, impedance function, and seepage speed to $z_{64°C}$ calculated from seepage speed and observations of the thermal data (Figure 11). A reasonable fit to the data is achieved with a mean excess fluid pressure of 20 kPa. This value is essentially identical to the 18 kPa excess fluid pressure measured in the sealed bore hole at ODP Site 1026, 6.3 km to the northeast [*Davis and Becker*, 2002]. This result is also consistent with numerical calculations of transient, coupled heat and fluid flow for the buried basement ridge [*Spinelli and Fisher*, 2004]. Because there is greater topographic relief and the presence of warm water above the sediment plain, one might expect the over-pressure at Baby Bare to be higher than that at ODP Site 1026, but any additional overpressure that is potentially generated by having a taller column of warm water in basement could be lost during fluid ascent through the edifice. Given the uncertainties in reservoir geometry, basement temperatures, and other factors, the consistency of these results is reassuring.

4.5. Longevity and Significance of Springs at Baby Bare

[36] Sediment cover and crustal permeability have a profound effect on the style and magnitude of heat loss on Baby Bare. As noted above, a few meters of sediment is sufficient to reduce significantly the rate of fluid seepage out of basaltic basement. Given the strong influence of sediment on fluid seepage, how long have Baby Bare springs been active and how long will they continue to flow?

[37] Approximately 10–15 m of sediment deposited along the ridge between Baby and Mama Bares was probably sufficient to force flow through these basaltic outcrops. Given that the oldest sediment at ODP Site 1026 is 1.58 Myr, which is substantially younger than the crustal age of about 3.6 Myr [*Davis et al.*, 1997a], and an average sedimentation rate of 290 m Myr^{-1} for the past 0.76 Myr, the hydrothermal system at Baby Bare could have operated for the past 1.2 Myr. A more conservative estimate requires 160 m of sediment to completely shut off flow along the ridge between these two seamounts [*Wheat and Mottl*, 1994], resulting in a longevity of 0.22 Myr and providing a greater driving force [e.g., *Fisher et al.*, 2003a]. Given the current turbidite sedimentation rate, the springs at Baby Bare should continue to seep for another 0.19 Myr, and detectable fluid flow through a sediment-covered Baby Bare will continue for an additional 0.55 Myr. These calculations illustrate that the longevity of springs on a ridge flank well exceed similar estimates for the continuous flow of hydrothermal fluids on mid-ocean ridges [e.g., *Fornari and Embley*, 1995].

[38] Aside from the sedimentation issue, is the Baby Bare system "representative" of typical ridge flank hydrothermal systems? Given an advective power output of 0.3 TW from 3- to 4-Myr crust [*Stein and Stein*, 1994] and the measured power output from Baby Bare (1.5 MW) relative to a similar sized area (0.1 MW), 2.1×10^5 Baby-Bare-type hydrothermal systems are required to deliver 0.3 TW. In general there would have to be a Baby-Bare-type hydrothermal system every 15 km^2 for the 3.3×10^6 km^2 of crust that is 3 to 4 Myr in age on a global basis, assuming ~58,500 km of mid-ocean ridges [*Baker et al.*, 1996] and an average crustal spreading rate of 55.7 mm yr^{-1} [*Henstock et al.*, 1993]. Clearly there is not one Baby Bare-type hydrothermal system every 15 km^2, yet heat must escape from the oceanic crust. To generate more heat loss relative to a Baby-Bare-type hydrothermal system, other more typical ridge flank hydrothermal systems must have (1) greater driving forces, which is possible if circulation penetrates more deeply into the crust, (2) higher permeability, or (3) shorter residence times or pathways. Thus the Baby Bare hydrothermal system is not a typical example of advective heat extraction on ridge flanks. Other systems with less sediment cover and/or greater volumetric fluid fluxes and power output on a regional basis are probably

more typical examples (e.g., Galapagos Mounds [*Williams et al.*, 1979; *Green et al.*, 1981; *Becker and Von Herzen*, 1983; *Bender*, 1983]).

5. Summary and Conclusions

[39] Historical evidence shows that basement topographic highs, outcrops, and seamounts can serve as crustal ventilators for hydrothermally altered seawater [e.g., *Lister*, 1972; *Thompson*, 1983]. Baby Bare outcrop is one such active crustal ventilator where springs result from a combination of highly permeable interconnected pathways in basaltic basement, topographically aided thermal buoyancy, and impermeable sediment that limits sites for recharge and discharge. Given the ridge-parallel orientation of faults, normal faults are probably the primary control for the egress of formation fluids from Baby Bare. One result of this fluid flow is a range of measured heat flow values from a background value of $\sim$0.27 W m^{-2} to as high as 490 W m^{-2}. The highest heat flow was measured in the sediment along the fault, highlighting the importance of faulting for ventilating the crust. There is no evidence that bottom seawater recharges anywhere into the crust at this site, which produces about an order of magnitude higher power output than a similar sized area in the region without crustal fluid ventilation. Instead, recharge for the Baby Bare seamount is thought to occur 52 km to the south-southwest, through another basement outcrop [*Wheat et al.*, 2000, 2002; *Fisher et al.*, 2003a]. Only a modest fraction of the power output at Baby Bare is advective, consistent with chemical modeling of ^{222}Rn/heat anomalies in springs and the overlying hydrothermal plume.

[40] Our analysis indicates that the 64°C isotherm extends above the surrounding turbidite plane and approaches within meters of the seafloor near the springs. This requires a net upward transport of lithospheric heat into the volcanic edifice. The role of sediment in limiting flow from the outcrop is illustrated particularly well along the western fault, where sediment prevents the formation of springs but does allow some seepage to occur. The role of sediment in directing fluid seepage at Baby Bare will likely continue for another $\sim$0.8 Myr, orders of magnitude longer than counterparts on mid-ocean ridges.

[41] Although the Baby Bare region experiences an anomalous high sedimentation rate, it is an excellent site to examine hydrothermal processes on ridge flanks. For example, the small size of Baby Bare provides a tractable target for a submersible study and the thick sediment coupled with a young crust produces a warm basement that reacts with formation fluids, allowing easy detection of fluid and heat flow. In addition semiburied edifices like this may provide an opportunity to monitor regional crustal hydrologic conditions such as the response to plate deformation without the expense of drilling deep boreholes. Although it will be more difficult to locate springs at other, more typical and cooler ridge flank hydrothermal sites where formation fluids are little altered chemically, such studies are required if we are to determine how fluid seepage through basement outcrops influences global fluxes of fluids, heat, and solutes.

Acknowledgments

[42] We are indebted to the experienced crews of the *Atlantis II* and DSV *Alvin* for collecting such a large sample suite even though the primary heat flow tool was destroyed on the second dive. We thank K Becker and an anonymous review for helpful comments that improved this manuscript. This work was supported by NSF OCE 9819454 and 0002031(to CGW), 9314632 and 9819974 (to MJM), 9819242 and 0001892 (AF), and 9456567 (to DK). GURU contribution 109. SOEST contribution 6471.

References

Baker, E. T., Y. J. Chen, and J. P. Morgan (1996), The relationship between near-axis hydrothermal cooling and the spreading rate of mid-ocean ridge, *Earth Planet. Sci. Lett.*, *142*, 137–145.

Becker, K., and E. E. Davis (2003), New evidence for age variation and scale effects of permeabilities of young oceanic crust from borehole thermal and pressure data, *Earth Planet. Sci. Lett.*, *210*, 499–508.

Becker, K., and R. P. Von Herzen (1983), Heat transfer through the sediments of the mounds hydrothermal area, Galapagos Spreading Center at 86°W, *J. Geophys. Res.*, *88*, 995–1008.

Becker, N. C., C. G. Wheat, M. J. Mottl, J. L. Karsten, and E. E. Davis (2000), A geological and geophysical investigation of Baby Bare, locus of a ridge-flank hydrothermal system in the Cascadia Basin, *J. Geophys. Res.*, *105*, 23,557–23,568.

Bender, M. L. (1983), Pore water chemistry of the mounds hydrothermal field, Galapagos Spreading Center: Results from Glomar Challenger piston coring, *J. Geophys. Res.*, *88*, 1049–1056.

Bredehoeft, J. D., and I. S. Papadopulos (1965), Rates of vertical groundwater movement estimated from the Earth's thermal profile, *Water Resour. Res.*, *1*, 325–328.

Bullard, E. C. (1954), The flow of heat through the floor of the Atlantic Ocean, *Proc. R. Soc. London, Ser. A*, *222*, 408–429.

Davis, E. E., and K. Becker (2002), Observations of natural-state fluid pressures and temperatures in young oceanic crust and inferences regarding hydrothermal circulation, *Earth Planet. Sci. Lett.*, *204*, 231–248.

Davis, E. E., et al. (1992), FlankFlux: An experiment to study the nature of hydrothermal circulation in young sea floor, *Can. J. Earth Sci.*, *29*, 925–952.

Davis, E. E., et al. (1997a), *Proceedings of the Ocean Drilling Program, Initial Reports*, vol. 168, Ocean Drill. Program, College Station, Tex.

Davis, E. E., D. S. Chapman, H. Villinger, S. Robinson, J. Grigel, A. Rosenberger, and D. Pribnow (1997b), Seafloor heat flow on the eastern flank of the Juan de Fuca Ridge: Data from "Flankflux" studies through 1995, *Proc. Ocean Drill. Program, Initial Rep.*, *168*, 22–33.

Davis, E. E., K. Wang, K. Becker, and R. E. Thomson (2000), Formation-scale hydraulic and mechanical properties of oceanic crust inferred from pore pressure response to periodic seafloor loading, *J. Geophys. Res.*, *105*, 13,423–13,435.

Davis, E. E., K. Wang, R. E. Thomson, K. Becker, and J. F. Cassidy (2001), An episode of seafloor spreading and associated plate deformation inferred from crustal fluid pressure transients, *J. Geophys. Res.*, *106*, 21,953–21,963.

Dymond, J., R. Cobler, L. Gordon, P. Biscaye, and C. Mathieu (1983), ^{226}Ra and ^{222}Rn contents of Galapagos Rift hydrothermal waters: The importance of low-temperature interactions with crustal rocks, *Earth Planet. Sci. Lett.*, *64*, 417–419.

Fisher, A. T. (1998), Permeability within basaltic oceanic crust, *Rev. Geophys.*, *36*, 143–182.

Fisher, A. T., and K. Becker (1995), Correlation between seafloor heat flow and basement relief: Observational and numerical examples and implications for upper crustal permeability, *J. Geophys. Res.*, *100*, 12,641–12,657.

Fisher, A. T., K. Becker, and E. E. Davis (1997), The permeability of young oceanic crust east of the Juan de Fuca Ridge, as determined using borehole thermal measurements, *Geophys. Res. Lett.*, *24*, 1311–1314.

Fisher, A. T., et al. (2003a), Hydrothermal recharge and discharge across 50 km guided by seamounts on a young ridge flank, *Nature*, *421*, 618–621.

Fisher, A. T., C. A. Stein, R. N. Harris, K. Wang, E. A. Silver, M. Pfender, M. Hutnak, A. Cherkaoui, R. Bodzin, and H. Villinger (2003b), Abrupt thermal transition reveals hydrothermal boundary and role of seamounts within the Cocos Plate, *Geophys. Res. Lett.*, *30*(11), 1550, doi:10.1029/2002GL016766.

Fornari, D. J., and R. W. Embley (1995), Tectonic and volcanic controls on hydrothermal processes at the mid-ocean ridge: An overview based on near-bottom and submersible studies, in *Seafloor Hydrothermal Systems: Physical, Chemical, Biological, and Geological Interactions*, *Geophys. Monogr. Ser.*, vol. 91, edited by S. Humphris et al., pp. 1–46, AGU, Washington, D. C.

Gendron, J. F., J. F. Todd, R. A. Feely, E. T. Baker, and D. C. Kadko (1994), Excess ^{222}Rn above the Cleft segment of the Juan de Fuca Ridge, *J. Geophys. Res.*, *99*, 5007–5015.

Giambalvo, E. R., A. T. Fisher, J. T. Martin, L. Darty, and R. P. Lowell (2000), Origin of elevated sediment permeability in a hydrothermal seepage zone, eastern flank of the Juan de Fuca Ridge, and implications for transport of fluid and heat, *J. Geophys. Res.*, *105*, 913–928.

Green, K. E., R. P. Von Herzen, and D. L. Williams (1981), The Galapagos Spreading Center at 86°W: A detailed geothermal field study, *J. Geophys. Res.*, *86*, 979–986.

Hardee, H. C., and D. W. Larson (1980), Thermal techniques for characterizing magma body geometries, *Geothermics*, *9*, 237–249.

Henstock, T. J., A. W. Woods, and R. S. White (1993), The accretion of oceanic crust by episodic sill intrusion, *J. Geophys. Res.*, *98*, 4143–4161.

Kadko, D., and W. Moore (1988), Radiochemical constraints on the crustal residence time of submarine hydrothermal fluids: Endeavour Ridge, *Geochim. Cosmochim. Acta*, *52*, 659–668.

Karsten, J. L., N. Becker, M. J. Mottl, and C. G. Wheat (1998), Petrology of Baby Bare and Mama Bare lavas, *Geophys. Res. Lett.*, *25*, 117–120.

Li, Y.-H., and S. Gregory (1974), Diffusion of ions in sea water and in deep-sea sediments, *Geochim. Cosmoshim. Acta*, *38*, 703–714.

Lister, C. R. B. (1972), On the thermal balance of a mid-ocean ridge, *Geophys. J. R. Astron. Soc.*, *26*, 515–535.

McManus, J., T. F. Nägler, C. Siebert, C. G. Wheat, and D. E. Hammond (2002), Oceanic molybdenum isotope fractionation: Diagenesis and hydrothermal ridge-flank alteration, *Geochem. Geophys. Geosyst.*, *3*, 1078, doi:10.1029/2002GC000356.

Mottl, M. J., et al. (1998), Warm springs discovered on 3.5 Ma-old oceanic crust, eastern flank of the Juan de Fuca Ridge, *Geology*, *26*, 51–54.

Rosenberg, N., J. E. Lupton, D. Kadko, R. Collier, M. D. Lilley, and H. Pak (1988), Estimation of heat and chemical fluxes from a seafloor hydrothermal vent field using radon measurements, *Nature*, *334*, 604–607.

Sclater, J. G., C. Jaupart, and D. Galson (1980), The heat flow through oceanic and continental crust and the heat loss of the earth, *Rev. Geophys.*, *18*, 269–311.

Sleep, N. H., and T. J. Wolery (1978), Egress of hot water from midocean ridge hydrothermal systems: Some thermal constraints, *J. Geophys. Res.*, *83*, 5913–5922.

Spinelli, G. A., and A. T. Fisher (2004), Hydrothermal circulation within topographically rough basaltic basement on the Juan de Fuca Ridge flank, *Geochem. Geophys. Geosyst.*, *5*, Q02001, doi:10.1029/2003GC000616.

Stein, C. A., and S. Stein (1994), Constraints on hydrothermal heat flux through the oceanic lithosphere from global heat flow, *J. Geophys. Res.*, *99*, 3081–3095.

Stein, J. S., A. T. Fisher, M. Langseth, W. Jin, G. Iturrino, and E. Davis (1998), Fine-scale heat flow, shallow heat sources, and decoupled circulation systems at two sea-floor hydrothermal sites, Middle Valley, northern Juan de Fuca Ridge, *Geology*, *26*, 1115–1118.

Thompson, G. (1983), Basalt-seawater interaction, in *Hydrothermal Processes at Seafloor Spreading Centers*, edited by P. A. Rona et al., pp. 225–278, Plenum, New York.

Thomson, R. E., E. E. Davis, and B. J. Burd (1995), Hydrothermal venting and geothermal heating in Cascadia Basin, *J. Geophys. Res.*, *100*, 6121–6141.

Villinger, H., and E. E. Davis (1987), A new reduction algorithm for marine heat flow measurements, *J. Geophys. Res.*, *92*, 12,846–12,856.

Villinger, H., I. Grevemeyer, N. Kaul, J. Hauschild, and M. Pfender (2002), Hydrothermal heat flux through aged oceanic crust: Where does the heat escape?, *Earth. Planet. Sci. Lett.*, *202*(1), 159–170.

Wang, K., J. He, and E. E. Davis (1997), Influence of basement topography on hydrothermal circulation in sediment-buried igneous oceanic crust, *Earth Planet. Sci. Lett.*, *146*, 151–164.

Wheat, C. G., and R. E. McDuff (1995), Mapping the fluid flow of the Mariana Mounds off-axis hydrothermal system: Pore water chemical tracers, *J. Geophys. Res.*, *100*, 8115–8131.

Wheat, C. G., and M. J. Mottl (1994), Hydrothermal circulation, Juan de Fuca Ridge eastern flank: Factors controlling basement water composition, *J. Geophys. Res.*, *99*, 3067–3080.

Wheat, C. G., and M. J. Mottl (2000), Composition of pore and spring waters from Baby Bare: Global implications of geochemical fluxes from a ridge flank hydrothermal system, *Geochim. Cosmochim. Acta.*, *64*, 629–642.

Wheat, C. G., M. J. Mottl, E. T. Baker, R. A. Feely, J. E. Lupton, F. J. Sansone, J. A. Resing, G. T. Lebon, and N. C. Becker (1997), Chemical anomalies in the water column from low-temperature hydrothermal venting on the eastern flank of the Juan de Fuca Ridge, *J. Geophys. Res.*, *102*, 15,433–15,446.

Wheat, C. G., H. Elderfield, M. J. Mottl, and C. Monnin (2000), Chemical composition of basement fluids within an oceanic ridge flank: Implications for along-strike and across-strike hydrothermal circulation, *J. Geophys. Res.*, *105*, 13,437–13,447.

Wheat, C. G., M. J. Mottl, and M. Rudniki (2002), Trace element and REE composition of a low-temperature ridge flank hydrothermal spring, *Geochim. Cosmochim. Acta*, *66*, 3693–3705.

Williams, D. L., K. Green, T. H. van Andel, R. P. Von Herzen, J. R. Dymond, and K. Crane (1979), The hydrothermal mounds of the Galapagos Rift: Observations with DSRV Alvin and detailed heat flow studies, *J. Geophys. Res.*, *84*, 7467–7484.